Science Advances
AAAS

Supplementary Materials for

Quantifying 3D live-cell membrane dynamics using dynamic metal-induced energy transfer spectroscopy (dynaMIET)

José Ignacio Gallea *et al.*

Corresponding author: Jörg Enderlein, jenderl@gwdg.de; Tao Chen, tao.chen@phys.uni-goettingen.de

Sci. Adv. **12**, eaed9613 (2026)
DOI: 10.1126/sciadv.aed9613

This PDF file includes:

Supplementary Text

Supporting Text 1. Correction of the photobleaching

The photobleaching of fluorophores during the measurement impacts the fluorescence intensity autocorrelation function gi,t (see Fig. S8). In our experiments, we noticed the photobleaching effects in the fluorophores of CellMask Deep Red and eGFP protein. As shown in Fig. S8, a discernible decay component is evident in the correlation curve, attributed to photobleaching. To mitigate the influence of photobleaching on gi,t, we performed a correction on the intensity time trace (I(t)) by applying a bi-exponential decay function:

$$z_{fit} = \sum_{i=1}^{2} a_i e^{-I(t)/t_i} + b \tag{S1}$$

where z_{fit} denotes the intensity decay curve, a_i represents the amplitudes, t_i refers to the decay constants, and b signifies an intensity offect. Consequently, we derived the relative intensity trace $I_{rel}(t) = I(t)/z_{fit}$ (Fig. S8). As illustrated in Fig. S8, the decay component attributed to photobleaching is effectively eliminated post-photobleaching correction.

Supporting Text 2. Determination of temporal resolution

The temporal resolution of measurement is contingent upon the count rates, which directly influence the accuracy of the lifetime and subsequent height calculations. According to previous studies, reliable accuracy in fast lifetime estimation necessitates a minimum of approximately 100 photon counts (*71, 72*). The photon count in each bin of the intensity trace is determined by factors such as fluorophore concentration, brightness, and excitation intensity. In our experiments involving four samples (GUV, PM, ER, NE), the count rates can easily exceed 1,000 kilo counts per second (k.c.p.s.) for GUV and PM samples. However, for ER and NE measurements, the count rates are lower, approximately 500 k.c.p.s. and 200 k.c.p.s., respectively. To ensure the accuracy of lifetime calculation, we employed a time bin width of 100 μs for GUV and PM samples, corresponding to approximately 100 photon counts per bin. For ER and NE measurements, we utilized a time bin width of 1 ms, corresponding to approximately 500 and 200 photon counts per bin, respectively. To assess the effect of photon count on the accuracy of lifetime and height calculations, we generated intensity traces (see Fig. S9) and their corresponding height traces (Fig. S9) using different time

bins ranging from 25 μs to 1 ms. As demonstrated in Fig. S9C and D, the intensity autocorrelation functions (iACFs) remained unaffected by the bin width. However, the height autocorrelation function (hACF) showed dependency on the bin width. Specifically, the amplitude of the hACFs did not vary notably when the photon counts per bin exceeded 40. Conversely, when the photon count dropped to 20 or lower, the amplitude of the hACF decreased substantially compared to other scenarios, resulting in an error of more than 1 nm in the membrane fluctuation amplitude.

Supporting Text 3. Statistics of ER dataset

When conducting a point measurement with a confocal microscope on the ER, positions are randomly selected to collect data. However, due to the sac-like and heterogeneous structures of the ER, the measured result represents a spatial average over all ER within the size of the excitation focus. Consequently, some ER regions outside the working distance of MIET are inadvertently included. This inclusion can lead to smaller measured values of fluctuation amplitude for ER, as movements form ER regions beyond the working distance of MIET do not contribute to height-related intensity fluctuations. To mitigate this effect, we implemented a lifetime threshold to exclude data points with large lifetimes, where quenching is not evident. Because lots of the ERs in these data points were placing out of the working distance of MIET, their lifetimes were dominated by these out-working-distance ER. We established this threshold based on the MIET calibration curve and brightness calibration curve of the of ER tracker Red fluorophore. As shown in Fig. S4, both calibration curves present steepest slopes for the height region below 65 nm (equivalent to 3.67 ns in lifetime), indicating the optimal working region of ER tracker Red is below 65nm. Consequently, we excluded data points with a lifetime exceeding 3.67 ns for the ER statistics. It is noteworthy that approximately 40% of data points were excluded from the statistics using this threshold.

Supporting Text 4. Calculation of brightness iso-surfaces

In this section we compute a 3D molecular brightness map $B(x, y, z)$ above a multilayer MIET substrate and then extract brightness iso-surfaces (level sets $B = \text{const}$). We proceed by first deriving the vectorial excitation focus produced by focusing a circularly polarized plane wave through a high numerical aperture objective, then by deriving the dipole emission in the stratified medium using the Weyl (plane-wave) representation, converting the stratified-medium emission into MIET height-

dependent radiation and dissipation, computing the collection efficiency of a high-NA objective, and finally combining excitation, effective quantum yield, and collection efficiency into a detected brightness model which we sample in 3D and from which we extract iso-surfaces.

First, let us compute the excitation field in the sample half-space (medium n) produced by a high-NA objective focusing a *circularly polarized* plane wave (diffraction-limited focusing). The focusing is modeled with an aplanatic Richards–Wolf representation (see Ref. (*74, 75*)) generalized to a stratified medium through the plane-wave decomposition and Fresnel transmission/reflection at the planar interfaces. The resulting field is evaluated on a cylindrical grid (ρ, z) and expanded into azimuthal Fourier–Bessel modes, consistent with the numerical implementation used to generate the coefficients $\{f_{xc}, f_{xs}, f_{yc}, f_{ys}, f_{zc}, f_{zs}\}$.

We adopt a Cartesian coordinate system where the planar multilayer stack lies in the xy-plane at $z = 0$. The excitation field is evaluated in the sample region of refractive index n occupying $0 < z < d$, bounded below by a stack of layers with refractive indices $\{n_{0,j}\}$ and thicknesses $\{d_{0,j}\}$, and (optionally) above by layers $\{n_{1,j}\}$ with thicknesses $\{d_{1,j}\}$. The excitation wavelength is λ_{ex} and we define the wavenumbers

$$k_0 = \frac{2\pi}{\lambda_{\mathrm{ex}}}, \qquad k_{0,j} = n_{0,j} k_0, \qquad k = n k_0, \qquad k_{1,j} = n_{1,j} k_0. \tag{S2}$$

The in-plane wavevector is $\mathbf{q} = (q_x, q_y)$ with magnitude $q = \|\mathbf{q}\|$. In the sample medium we define the normalized in-plane spatial frequency

$$s = \frac{q}{k_{0,1}}, \qquad s_0 = \sin\chi, \qquad c_0 = \cos\chi, \qquad ss = \frac{n_{0,1}}{n} s_0, \qquad cc = \sqrt{1 - ss^2}, \tag{S3}$$

where $\chi \in [0, \chi_{\max}]$ is the convergence angle in the immersion medium of refractive index $n_{0,1}$, and

$$\chi_{\max} = \arcsin\left(\frac{\mathrm{NA}}{n_{0,1}}\right). \tag{S4}$$

Thus, a plane-wave component labeled by χ has in the sample medium an in-plane factor $k\, ss$ and a longitudinal factor $k\, cc$.

Propagation through the multilayer is handled by Fresnel coefficients for p- and s-polarized components. Denoting the (complex) transmission and reflection amplitudes into the sample by $t_p(\chi), t_s(\chi)$ and the corresponding effective reflection amplitudes within the sample by $r_p(\chi), r_s(\chi)$ (including multiple reflections across the sample thickness d), the downward- and upward-propagating

contributions at axial coordinate z are carried by the phases

$$\Phi_1(\chi; z) = k\, cc\, z - k_{0,1} c_0\, z_f, \qquad \Phi_2(\chi; z) = k\, cc\, (2d - z) - k_{0,1} c_0\, z_f, \tag{S5}$$

where z_f is the axial focus offset (positive z_f shifts the nominal focus relative to the interface). These phases correspond to the transmitted field and the field reflected from the upper boundary, respectively.

The incident field is specified in the objective BFP as a circularly polarized plane wave with electric field amplitude E_0 and pupil weight function $A(\chi)$. For an aplanatic objective we include the standard apodization $\sqrt{\cos\chi}$. The scalar pupil weight used in the angular spectrum integral is therefore

$$W(\chi) = A(\chi)\, \sqrt{\cos\chi}\, \sin\chi, \tag{S6}$$

where the additional $\sin\chi$ factor comes from the solid-angle element in the Debye integral.

Lateral displacement of the focal spot by ρ_0 at azimuth ψ_0 is represented by the standard phase factor

$$\exp\big(i\, k\, ss\, \rho_0 \cos(\psi - \psi_0)\big). \tag{S7}$$

We describe polarization using the local p/s basis for each plane-wave component. Let the pupil azimuth be ψ and denote $c_\psi = \cos\psi$ and $s_\psi = \sin\psi$. For each component the unit vectors in the sample are

$$\hat{\mathbf{s}} = (-s_\psi,\, c_\psi,\, 0), \qquad \hat{\mathbf{p}} = (cc\, c_\psi,\, cc\, s_\psi,\, -ss), \tag{S8}$$

so that $\hat{\mathbf{p}}$ lies in the meridional plane and $\hat{\mathbf{s}}$ is orthogonal to it.

A right-handed circularly polarized field in the BFP is taken as

$$\mathbf{e}^{(+)}_{\mathrm{BFP}} = \frac{1}{\sqrt{2}}\, (\hat{\mathbf{x}} + i\, \hat{\mathbf{y}})\,, \tag{S9}$$

and its projection onto the local p/s basis determines the p and s weights for each (χ, ψ) component. Equivalently, and most conveniently for implementation, we exploit linearity: the focused field for circular polarization is the superposition of the x- and y-polarized focused fields with a $\pi/2$ phase shift,

$$\boxed{\mathbf{E}^{(+)}_{\mathrm{ex}}(\rho, \varphi, z) = \frac{1}{\sqrt{2}} \left[\mathbf{E}^{(x)}_{\mathrm{ex}}(\rho, \varphi, z) + i\, \mathbf{E}^{(y)}_{\mathrm{ex}}(\rho, \varphi, z)\right].} \tag{S10}$$

Here $\mathbf{E}_{\mathrm{ex}}^{(x)}$ is the field produced by an x-polarized BFP input, and $\mathbf{E}_{\mathrm{ex}}^{(y)}$ is obtained by rotating the input linear polarization by 90° in the BFP (equivalently $\varphi \mapsto \varphi + \pi/2$ at fixed ρ for the same pupil function).

Because the system is cylindrically stratified (planar interfaces) and the pupil dependence is 2π-periodic in ψ, it is convenient to represent each Cartesian component of the excitation field by a truncated Fourier series in the observation azimuth φ,

$$E_x(\rho,\varphi,z) = f_{xc}^{(0)}(\rho,z) + \sum_{m=1}^{m_{\max}} \left[f_{xc}^{(m)}(\rho,z)\cos(m\varphi) + f_{xs}^{(m)}(\rho,z)\sin(m\varphi) \right], \tag{S11}$$

$$E_y(\rho,\varphi,z) = f_{yc}^{(0)}(\rho,z) + \sum_{m=1}^{m_{\max}} \left[f_{yc}^{(m)}(\rho,z)\cos(m\varphi) + f_{ys}^{(m)}(\rho,z)\sin(m\varphi) \right], \tag{S12}$$

$$E_z(\rho,\varphi,z) = f_{zc}^{(0)}(\rho,z) + \sum_{m=1}^{m_{\max}} \left[f_{zc}^{(m)}(\rho,z)\cos(m\varphi) + f_{zs}^{(m)}(\rho,z)\sin(m\varphi) \right]. \tag{S13}$$

The coefficient fields $f_{\bullet c}^{(m)}(\rho,z)$ and $f_{\bullet s}^{(m)}(\rho,z)$ are obtained from angular-spectrum integrals over χ involving Bessel functions $J_m(k\,ss\,\rho)$ and the stratified-medium amplitudes $t_{p,s}(\chi)$ and $r_{p,s}(\chi)$. In practice these coefficients are computed numerically and the full field for any observation azimuth φ is reconstructed by evaluating the truncated series.

For circular polarization we construct two linear-polarization reconstructions separated by $\pi/2$ in azimuth and form the complex superposition in Eq. (S10). Explicitly, letting

$$\mathbf{E}_{\mathrm{ex}}^{(y)}(\rho,\varphi,z) = \mathbf{E}_{\mathrm{ex}}^{(x)}(\rho,\varphi+\tfrac{\pi}{2},z), \tag{S14}$$

we obtain

$$\mathbf{E}_{\mathrm{ex}}^{(+)}(\rho,\varphi,z) = \frac{1}{\sqrt{2}}\left[\mathbf{E}_{\mathrm{ex}}^{(x)}(\rho,\varphi,z) + i\,\mathbf{E}_{\mathrm{ex}}^{(x)}(\rho,\varphi+\tfrac{\pi}{2},z) \right]. \tag{S15}$$

This construction matches the numerical procedure of evaluating the coefficient expansion at two azimuths separated by $\pi/2$ and combining them with a quadrature phase shift.

The local excitation intensity is computed from the focused field as

$$I_{\mathrm{ex}}(\mathbf{r}) = \frac{n\,\varepsilon_0 c}{2}\left\|\mathbf{E}_{\mathrm{ex}}^{(+)}(\mathbf{r})\right\|^2, \qquad \mathbf{r} = (\rho,\varphi,z). \tag{S16}$$

For a molecular absorption dipole $\boldsymbol{\mu}_{\mathrm{abs}} = \mu_{\mathrm{abs}}\hat{\mathbf{u}}$, the excitation rate scales as

$$R_{\mathrm{ex}}(\mathbf{r},\hat{\mathbf{u}}) \propto \left|\hat{\mathbf{u}}\cdot\mathbf{E}_{\mathrm{ex}}^{(+)}(\mathbf{r})\right|^2. \tag{S17}$$

If the absorber samples orientations rapidly (isotropic absorption), the orientational average yields

$$\left\langle \left| \hat{\mathbf{u}} \cdot \mathbf{E}_{\mathrm{ex}}^{(+)}(\mathbf{r}) \right|^2 \right\rangle_{\hat{\mathbf{u}}} = \frac{1}{3} \left\| \mathbf{E}_{\mathrm{ex}}^{(+)}(\mathbf{r}) \right\|^2, \tag{S18}$$

and we therefore take $R_{\mathrm{ex}}(\mathbf{r}) \propto \|\mathbf{E}_{\mathrm{ex}}^{(+)}(\mathbf{r})\|^2$ in the isotropic-absorption limit.

Next, we derive the emission from a classical electric dipole with dipole amplitude vector $\mathbf{p}$ placed at $\mathbf{r}_0 = (\boldsymbol{\rho}_0, h)$, where h denotes the emitter height above the reference interface. We formulate dipole emission in the stratified medium using the Weyl (plane-wave) representation of the dyadic Green tensor together with generalized plane-wave Fresnel reflection and transmission coefficients. We state the required relations, describe how we separate radiative and nonradiative channels (including the MIET contribution), compute collection efficiency, and combine excitation, quantum yield, and collection into a single brightness model $b(x, y, h)$ from which we extract brightness iso-surfaces.

The scalar Weyl identity for a spherical wave reads

$$\frac{e^{ikR}}{R} = \frac{i}{2\pi} \int_{\mathbb{R}^2} \frac{1}{w} \exp\big(i\mathbf{q} \cdot (\boldsymbol{\rho} - \boldsymbol{\rho}_0) + iw|z - h|\big)\, d^2\mathbf{q}, \qquad w = \sqrt{k^2 - q^2}, \tag{S19}$$

and allows us to express the dipole fields as an angular spectrum of plane waves labeled by the in-plane wavevector $\mathbf{q}$. For each $\mathbf{q}$ we adopt the orthonormal polarization basis consisting of the s (TE) unit vector

$$\hat{\mathbf{e}}_s(\mathbf{q}) = \frac{1}{q}(-q_y, q_x, 0), \tag{S20}$$

and the p (TM) unit vectors for upward (+) and downward (−) propagation in medium j,

$$\hat{\mathbf{e}}_{p,j}^{\pm}(\mathbf{q}) = \frac{1}{k_j q}\big(\pm w_j q_x,\ \pm w_j q_y,\ -q^2\big), \tag{S21}$$

which satisfy $\hat{\mathbf{e}}_{p,j}^{\pm} \cdot \mathbf{k}_j^{\pm} = 0$ with $\mathbf{k}_j^{\pm} = (q_x, q_y, \pm w_j)$.

At each interface between media j and k we use the standard Fresnel reflection and transmission coefficients for s and p polarizations:

$$r_s^{(jk)} = \frac{w_j - w_k}{w_j + w_k}, \qquad r_p^{(jk)} = \frac{\varepsilon_k w_j - \varepsilon_j w_k}{\varepsilon_k w_j + \varepsilon_j w_k}, \tag{S22}$$

$$t_s^{(jk)} = \frac{2w_j}{w_j + w_k}, \qquad t_p^{(jk)} = \frac{2\varepsilon_k w_j}{\varepsilon_k w_j + \varepsilon_j w_k}, \tag{S23}$$

where $\varepsilon_j = n_j^2 \varepsilon_0$. For a finite-thickness layer m of thickness h_m between medium 1 and medium 2 we compute generalized reflection and transmission coefficients for each $\mathbf{q}$ and polarization via Fabry–Pérot (transfer- or scattering-matrix) recursions. For the two-interface stack (medium 1 — layer m — medium 2) we write

$$R_\sigma(\mathbf{q}) = \frac{r_\sigma^{(1m)} + r_\sigma^{(m2)} e^{2iw_m h_m}}{1 + r_\sigma^{(1m)} r_\sigma^{(m2)} e^{2iw_m h_m}}, \tag{S24}$$

$$T_\sigma(\mathbf{q}) = \frac{t_\sigma^{(1m)} t_\sigma^{(m2)} e^{iw_m h_m}}{1 + r_\sigma^{(1m)} r_\sigma^{(m2)} e^{2iw_m h_m}}, \tag{S25}$$

with $\sigma \in \{s, p\}$. We evaluate $R_\sigma(\mathbf{q})$ and $T_\sigma(\mathbf{q})$ at $q = k_1 s$ when the emitter is in medium 1, using the normalized in-plane variable $s = q/k_1$.

We model a focused excitation field with plane-polarized light along the x-axis in the back focal plane (BFP) of the objective. We compute the vectorial focused excitation $\mathbf{E}_{\text{ex}}(x, y, z)$ from the BFP field via the Richards–Wolf integral and form the excitation rate $R_{\text{ex}}(\mathbf{r}) \propto \|\mathbf{E}_{\text{ex}}(\mathbf{r})\|^2$ for isotropic absorption or $R_{\text{ex}}(\mathbf{r}) \propto |\hat{\mathbf{u}} \cdot \mathbf{E}_{\text{ex}}(\mathbf{r})|^2$ for a fixed dipole orientation $\hat{\mathbf{u}}$.

Using the angular-spectrum representation and the generalized transmission coefficients we express the transmitted electric field into the substrate (medium 2, $z < 0$) as

$$\mathbf{E}^{(T)}(\mathbf{r}) = \frac{i}{2\pi} \int_{\mathbb{R}^2} \frac{1}{w_2} e^{i\mathbf{q}\cdot(\boldsymbol{\rho}-\boldsymbol{\rho}_0)} e^{iw_1 h} e^{-iw_2 z} \times \left[T_p(\mathbf{q})\, \hat{\mathbf{e}}_{p,2}^{-} \big(\hat{\mathbf{e}}_{p,1}^{+} \cdot \mathbf{p}\big) + T_s(\mathbf{q})\, \hat{\mathbf{e}}_s \big(\hat{\mathbf{e}}_s \cdot \mathbf{p}\big) \right] d^2\mathbf{q}, \tag{S26}$$

and analogous angular-spectrum expressions describe the reflected field in the upper half-space using $R_s(\mathbf{q})$ and $R_p(\mathbf{q})$. We compute power fluxes via the Poynting vector and we construct the dyadic Green tensor by summing the homogeneous-space contribution and the reflection-dependent part obtained from these plane-wave expansions.

We evaluate the spontaneous-emission decay rate from the dyadic Green tensor at the dipole position. For a dipole $\mathbf{p} = p\hat{\mathbf{u}}$ we use

$$S(\mathbf{r}_0, \hat{\mathbf{u}}) = \frac{2\omega^2}{\hbar \varepsilon_0 c^2}\, \mathbf{p} \cdot \mathrm{Im}\big[\mathbf{G}(\mathbf{r}_0, \mathbf{r}_0)\big] \cdot \mathbf{p}, \tag{S27}$$

and we separate the Green tensor into the homogeneous-space part and a reflected part that depends on the multilayer reflection coefficients. After projecting onto dipole orientations and carrying out angular-spectrum manipulations we obtain one-dimensional integrals over s for the normalized

decay rates S/S_0, where S_0 is the decay rate in an infinite homogeneous medium of refractive index n_1. For a dipole oriented perpendicular to the interface ($\hat{\mathbf{u}} = \hat{\mathbf{z}}$) we obtain

$$\frac{S_\perp(h)}{S_0} = 1 + \frac{3}{2}\,\mathrm{Re}\int_0^\infty \frac{s^3}{s_z}\,R_p(s)\,e^{2ik_1 h s_z}\,ds, \tag{S28}$$

and for a dipole oriented parallel to the interface ($\hat{\mathbf{u}} \perp \hat{\mathbf{z}}$) we have

$$\frac{S_\parallel(h)}{S_0} = 1 + \frac{3}{4}\,\mathrm{Re}\int_0^\infty \left[sR_s(s) + s_z R_p(s)\right] e^{2ik_1 h s_z}\,ds. \tag{S29}$$

Here $R_s(s)$ and $R_p(s)$ denote the generalized Fresnel reflection coefficients evaluated at $q = k_1 s$, and

$$s_z = \begin{cases} \sqrt{1-s^2}, & 0 \le s \le 1, \\ i\sqrt{s^2-1}, & s > 1, \end{cases} \tag{S30}$$

with the branch convention $\mathrm{Im}\, s_z \ge 0$. For an isotropic orientational ensemble we compute the orientational average

$$S_{\mathrm{iso}}(h) = \tfrac{1}{3}S_\perp(h) + \tfrac{2}{3}S_\parallel(h). \tag{S31}$$

We separate radiative and nonradiative contributions by splitting the angular-spectrum integrals into propagating ($0 \le s \le 1$ in medium 1, or equivalently $q \le k_2$ in medium 2 as appropriate) and evanescent ($s > 1$) domains. The total decay rate may be written

$$S(h) = S^{\mathrm{prop}}(h) + S^{\mathrm{ev}}(h), \tag{S32}$$

where the propagating part corresponds to channels that radiate into the far field and the evanescent part captures near-field coupling that can be absorbed as Ohmic loss in metallic layers (MIET) or coupled into guided and substrate-propagating channels.

We denote by $N(h, \hat{\mathbf{u}})$ the power (energy per unit time) transmitted into the lower half-space (the substrate). We compute N by integrating the transmitted Poynting flux of the angular spectrum over the substrate's propagating domain:

$$N(h, \hat{\mathbf{u}}) = \int_{\|\mathbf{q}\| \le k_2} \mathcal{N}(\mathbf{q}; h, \hat{\mathbf{u}})\,d^2\mathbf{q}, \tag{S33}$$

where $\mathcal{N}(\mathbf{q}; h, \hat{\mathbf{u}})$ is the differential power per $\mathbf{q}$-mode derived from the transmitted-field angular-spectrum coefficients $T_s(\mathbf{q})$ and $T_p(\mathbf{q})$ and from the dipole projections onto the s and p basis vectors. We convert this power into an equivalent radiative decay rate into the substrate,

$$S_{\mathrm{rad},\downarrow}(h, \hat{\mathbf{u}}) = \frac{N(h, \hat{\mathbf{u}})}{\hbar\omega}. \tag{S34}$$

Analogous expressions give the upward radiative rate $S_{\mathrm{rad},\uparrow}(h, \hat{\mathbf{u}})$ and the total radiative rate

$$S_{\mathrm{rad}}(h, \hat{\mathbf{u}}) = S_{\mathrm{rad},\uparrow}(h, \hat{\mathbf{u}}) + S_{\mathrm{rad},\downarrow}(h, \hat{\mathbf{u}}). \tag{S35}$$

We then define the MIET-induced nonradiative rate as the difference between the total power dissipated and the radiative rate,

$$S_{\mathrm{nrad,MIET}}(h, \hat{\mathbf{u}}) = S_{\mathrm{tot}}(h, \hat{\mathbf{u}}) - S_{\mathrm{rad}}(h, \hat{\mathbf{u}}). \tag{S36}$$

We combine the environment-dependent rates with intrinsic (free-space) radiative and nonradiative rates to obtain an effective quantum yield as a function of height h. Let the free-space total decay be $S_0 = S_{0,\mathrm{rad}} + S_{0,\mathrm{nrad,int}}$ and define the intrinsic quantum yield

$$\Phi_0 = \frac{S_{0,\mathrm{rad}}}{S_0}. \tag{S37}$$

Then the intrinsic nonradiative rate is

$$S_{0,\mathrm{nrad,int}} = S_{0,\mathrm{rad}} \frac{1 - \Phi_0}{\Phi_0}. \tag{S38}$$

In the presence of the MIET stack the total decay becomes

$$S_{\mathrm{tot}}(h) = S_{\mathrm{rad}}(h) + S_{\mathrm{nrad,MIET}}(h) + S_{0,\mathrm{nrad,int}}, \tag{S39}$$

and we define the effective, height-dependent quantum yield

$$\Phi(h) = \frac{S_{\mathrm{rad}}(h)}{S_{\mathrm{rad}}(h) + S_{\mathrm{nrad,MIET}}(h) + S_{0,\mathrm{nrad,int}}}. \tag{S40}$$

When dipole-orientation dependence is relevant we retain the implicit $\hat{\mathbf{u}}$ dependence and perform orientation averages only when physically justified.

We compute the collection efficiency $C(h)$ of the detection optics assuming detection through the substrate (downward direction) with an objective of numerical aperture NA immersed in medium 2 (refractive index n_2). The maximum collection angle in medium 2 is

$$\theta_{\max} = \arcsin\left(\frac{\mathrm{NA}}{n_2}\right). \tag{S41}$$

For each direction (θ, ϕ) in the substrate the angular-dependent differential radiated power is $\frac{dN}{d\Omega}(\theta, \phi; h)$. We therefore define the collection efficiency into the objective as

$$C(h) = \frac{\int_0^{2\pi} \int_0^{\theta_{\max}} \frac{dN}{d\Omega}(\theta, \phi; h)\ \sin\theta\, d\theta\, d\phi}{\int_0^{2\pi} \int_0^{\pi/2} \frac{dN}{d\Omega}(\theta, \phi; h)\ \sin\theta\, d\theta\, d\phi}. \tag{S42}$$

Equivalently, in the plane-wave representation we express $C(h)$ as an integral over $\mathbf{q}$ in medium 2: the NA acceptance corresponds to $\|\mathbf{q}\| \le k_0 \mathrm{NA}$, and the full substrate propagating domain corresponds to $\|\mathbf{q}\| \le k_2$. Thus

$$C(h) = \frac{\int_{\|\mathbf{q}\| \le k_0 \mathrm{NA}} \mathcal{N}(\mathbf{q}; h)\, d^2\mathbf{q}}{\int_{\|\mathbf{q}\| \le k_2} \mathcal{N}(\mathbf{q}; h)\, d^2\mathbf{q}}, \tag{S43}$$

where $\mathcal{N}(\mathbf{q}; h)$ is the differential transmitted power per $\mathbf{q}$-mode.

Finally, we combine excitation, effective quantum yield, and collection efficiency into a detected photon-rate (brightness) model. Up to an overall instrument constant C_{inst} that accounts for laser power, detector efficiency, filter transmission, and other throughput factors, we define the detected brightness of a single molecule by the scalar $b(\mathbf{r})$. We write

$$b(\mathbf{r}) = C_{\mathrm{inst}}\ R_{\mathrm{ex}}(\mathbf{r})\ \Phi(h)\ C(h). \tag{S44}$$

For isotropic absorption $R_{\mathrm{ex}}(\mathbf{r}) \propto \|\mathbf{E}_{\mathrm{ex}}(\mathbf{r})\|^2$, so we commonly use

$$b(x, y, h) \propto \|\mathbf{E}_{\mathrm{ex}}(x, y, h)\|^2\ \Phi(h)\ C(h). \tag{S45}$$

For a fixed dipole orientation $\hat{\mathbf{u}}$ we instead use

$$b(\mathbf{r}, \hat{\mathbf{u}}) \propto \left|\hat{\mathbf{u}} \cdot \mathbf{E}_{\mathrm{ex}}(\mathbf{r})\right|^2\ \Phi(h, \hat{\mathbf{u}})\ C(h, \hat{\mathbf{u}}), \tag{S46}$$

and we perform orientation averaging only where appropriate.

We define brightness iso-surfaces at level b_* as the set

$$\mathcal{S}(b_*) = \{(x, y, h)\ :\ b(x, y, h) = b_*\}. \tag{S47}$$

In numerical practice we compute b on a 3D grid and extract $\mathcal{S}(b_*)$ using a marching-cubes or equivalent isosurface-extraction algorithm. For visualization and for comparisons across experimental conditions we often select a relative threshold

$$b_* = \beta\, b_{\max}, \qquad 0 < \beta < 1, \tag{S48}$$

and plot $\mathcal{S}(\beta b_{\max})$, which highlights the spatial region that contributes a chosen fraction of the maximal detected brightness.

We summarize the computational steps we perform:

1. We calculate the focused excitation field $\mathbf{E}_{\mathrm{ex}}(x, y, h)$ using the Debye–Wolf integral for a circularly BFP field and form $R_{\mathrm{ex}}(\mathbf{r})$ either for a fixed dipole orientation or averaged over orientations.

2. We compute generalized reflection and transmission coefficients $R_s(\mathbf{q}), R_p(\mathbf{q}), T_s(\mathbf{q}), T_p(\mathbf{q})$ for the MIET stack using transfer- or scattering-matrix recursions for each $\mathbf{q}$.

3. We evaluate $S_\perp(h)$ and $S_\parallel(h)$ from the one-dimensional integrals (S28) and (S29), and form $S_{\mathrm{iso}}(h)$ when required.

4. We compute radiative power $N(h)$ into the substrate and into the upper half-space from the angular-spectrum transmitted and reflected fields, convert these powers to radiative decay rates $S_{\mathrm{rad},\downarrow}(h)$, $S_{\mathrm{rad},\uparrow}(h)$, and compute $S_{\mathrm{nrad,MIET}}(h)$ by subtraction.

5. We compute the height-dependent effective quantum yield $\Phi(h)$ from (S40) using the known intrinsic quantum yield Φ_0.

6. We compute the collection efficiency $C(h)$ by integrating the substrate radiated power over the NA acceptance (or the equivalent $\mathbf{q}$-domain).

7. We evaluate $b(x, y, h)$ from (S44) on a 3D grid and extract brightness iso-surfaces $\mathcal{S}(b_*)$ for chosen thresholds b_*.

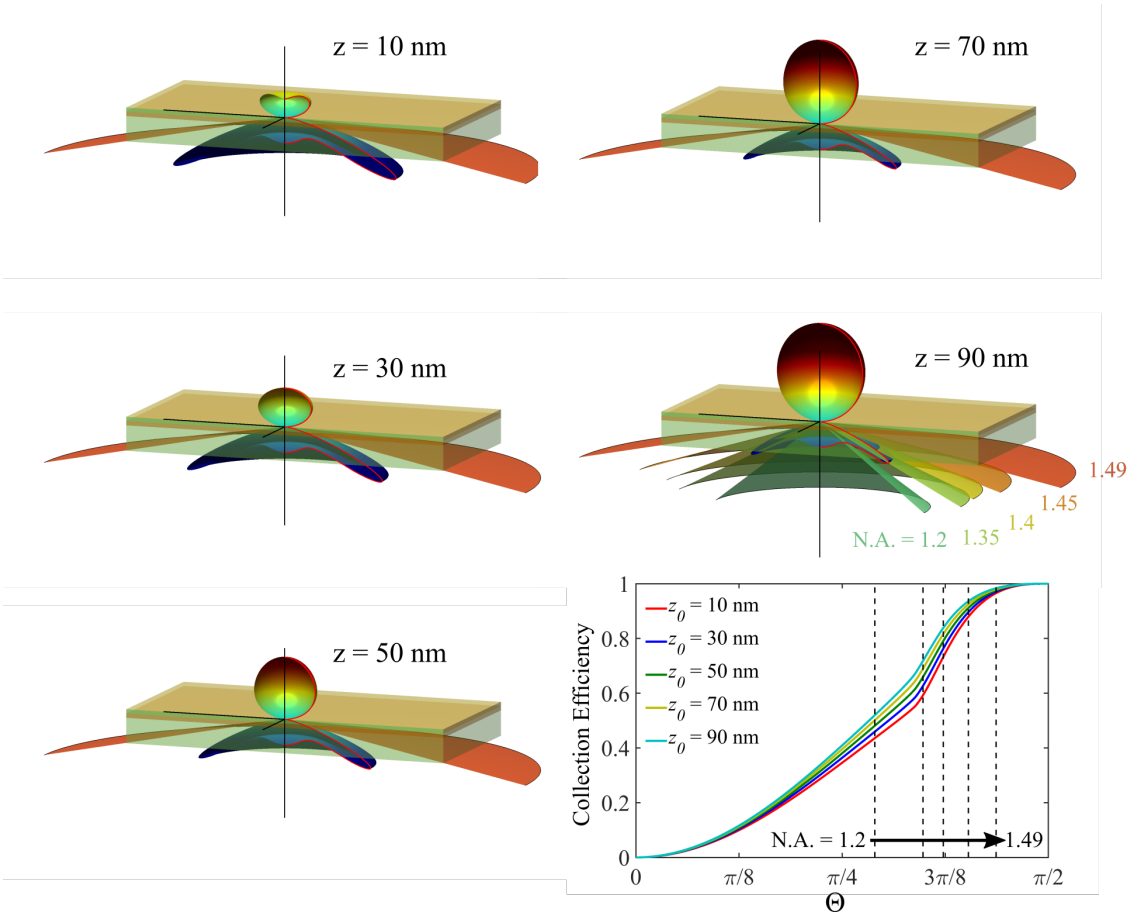

Figure S1: Angular distribution of freely rotating dipoles placed at various axial positions (z = 10, 30, 50, 70 & 90 nm from the MIET substrate. The cone shows the collection angle of an objective with N.A.= 1.49. The graph shows the collection efficiency of radiative photons in the bottom half space (towards the objective) as a function of collection cone angle Θ.

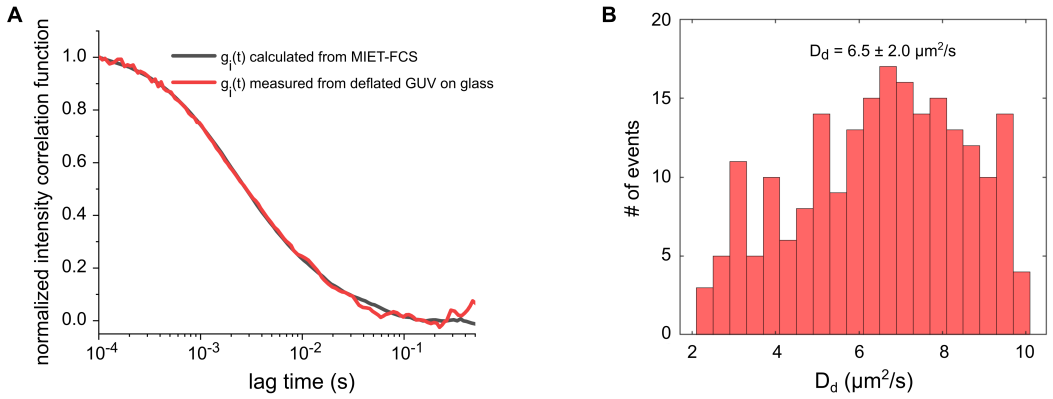

Figure S2: **Conventional FCS on deflated GUVs.** (A) Normalized intensity correlation function gi(t) calculated from dynaMIET, the data were measured from a deflated GUV on MIET substrate (black curve), and the normalized intensity correlation function gi(t) was directly measured from the deflated GUV on glass (red curve). (B) Histogram illustrating the diffusion coefficients Dd measured from the deflated GUV on glass. The mean Dd is 6.5 ± 2.0 $\mu m^2/s$ (mean ± SD, n = 214).

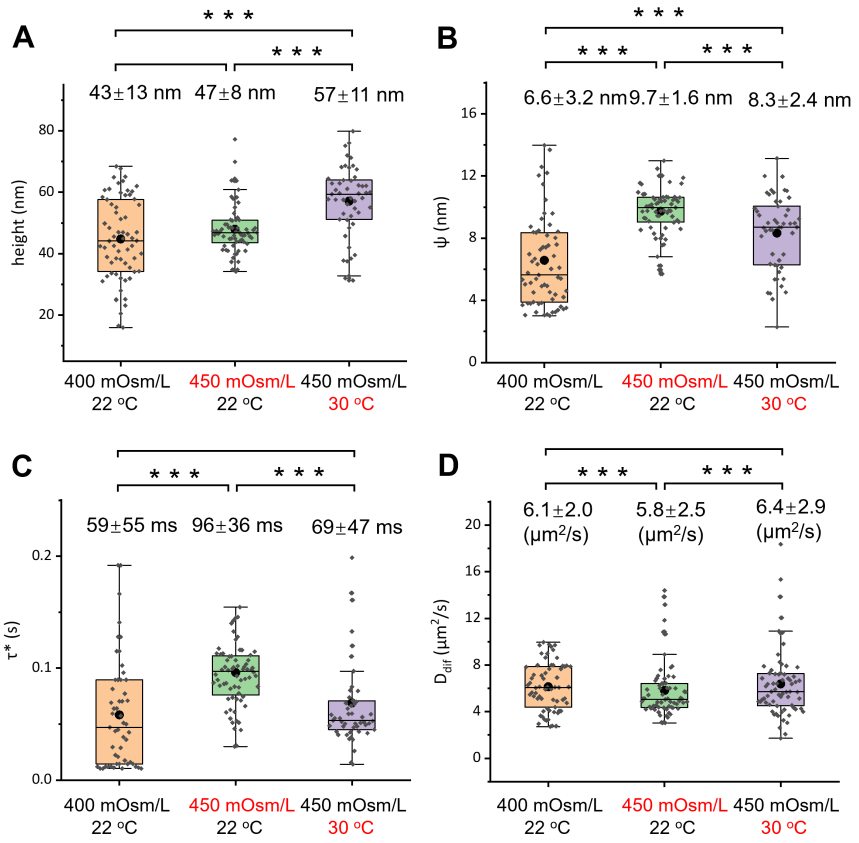

Figure S3: **dynaMIET measurement on GUVs under different conditions.** (A, B, C, D) Box plots for the mean height (A), height correlation amplitude ψ (B), relaxation time $\tau*$ (C), and diffusion coefficient D_{dif} (D) for GUV under different experimental conditions. Box plots indicate the 25th–75th quantiles (box), median (black line), mean (black dot), and whiskers (minima to maxima). Measurements were performed with $n = 68$ independent measurements from 3 independent experiments for GUVs at 22 °C in 450 mOsm/L PBS solution, $n = 51$ independent measurements from 4 independent experiments for GUVs at 30 °C in 400 mOsm/L PBS solution, and $n = 65$ independent measurements from 4 independent experiments for deflated GUVs at 22 °C in 450 mOsm/L PBS solution. Mean values and standard errors are indicated. Significance levels P were evaluated by a Mann-Whitney U-test: $P < 0.001$ ($\star\star\star$), $P < 0.01$ ($\star\star$), $P < 0.05$ ($\star$).

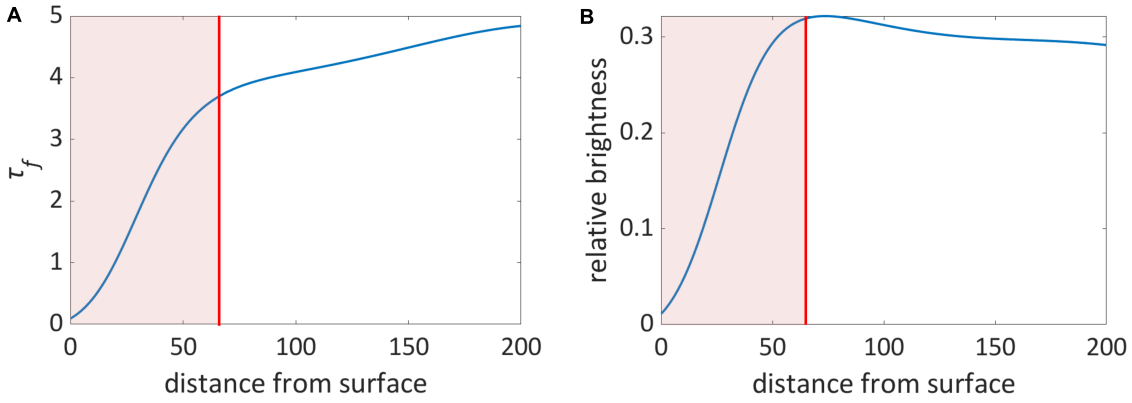

Figure S4: **Calculated calibration curves of dye ER Tracker Red.** (A) Calculated fluorescence lifetime of an ER Tracker Red as a function of its distance from the surface of a MIET substrate, (B) and calculated relative brightness of an ER Tracker Red as a function of its distance from the surface of a MIET substrate. The MIET substrate consists multiple layers: 10 nm silica, 1 nm titanium, 10 nm gold film, 2 nm titanium, and glass coverslip. All calculations were performed for an emitter with maximum emission wavelength of 590 nm, fluorescence quantum yield of 0.9, free-space lifetime of 4.6, and random orientation. The red lines indicate the threshold for the statistics of ER dataset. The free-space lifetime of 4.6 was measured from ER Tracker Red dye in cell on a glass surface and the quantum yield of 0.9 take the values from published reference (*76*).

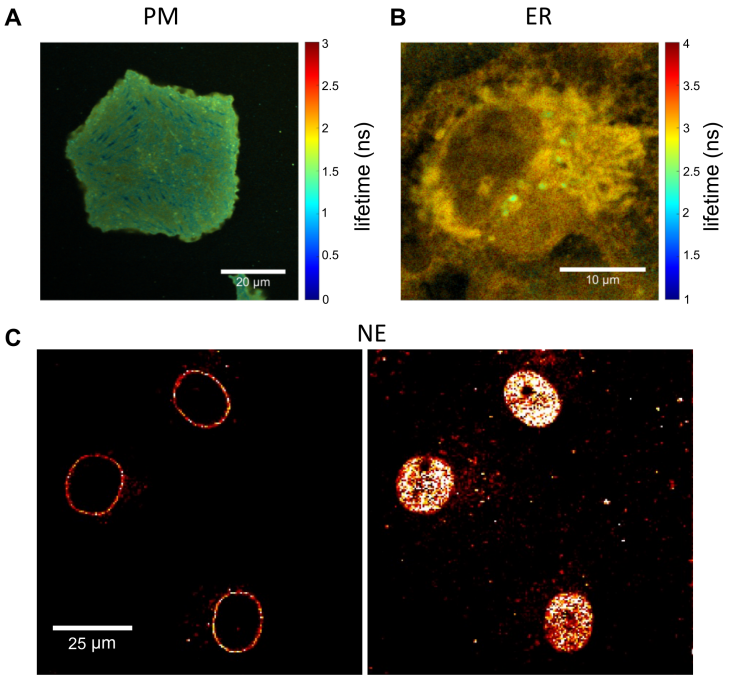

Figure S5: **Fluorescence (lifetime) images of COS7 cells measured on MIET substrate.** (A, B) Fluorescence lifetime images of COS7 cells labeled with CellMask to visualize the PM (A) and with ER-Tracker to label the ER (B). (C) Fluorescence image of COS7 cells expressing GFP–Nup153. Images were acquired by confocal scanning at the center of the cell nucleus (left) and at the bottom of the cell nucleus (right).

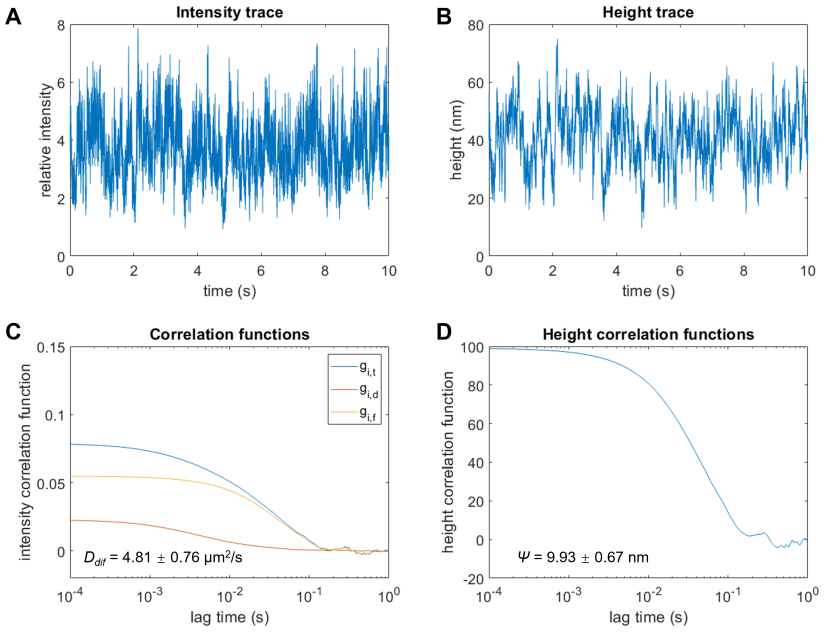

Figure S6: **Simulation for a fluctuating membrane with high labeling above a gold surface.** (A) Simulated fluorescence intensity trace (B) and height trace. (C) Calculated intensity correlation curves. (D) Calculated height correlation curve. The simulation methodology is the same as that used in Fig. 1 of the main text, except that the particle concentration was increased to C = 150 particles/μm^2, corresponding to an average of approximately 43 particles within the confocal volume.

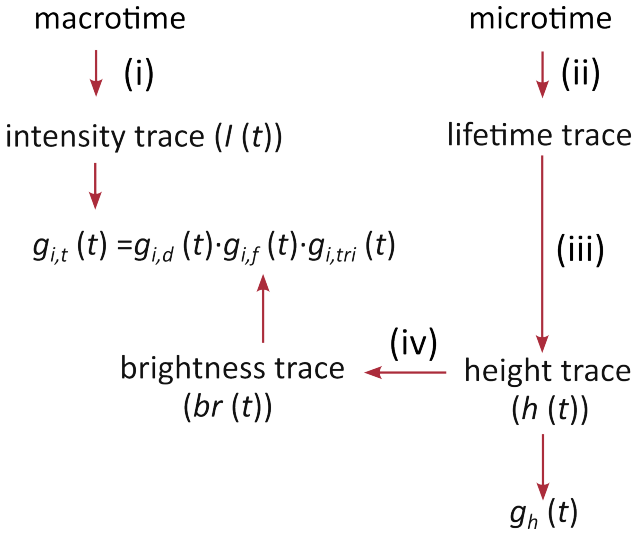

Figure S7: dynaMIET analysis flow chart.

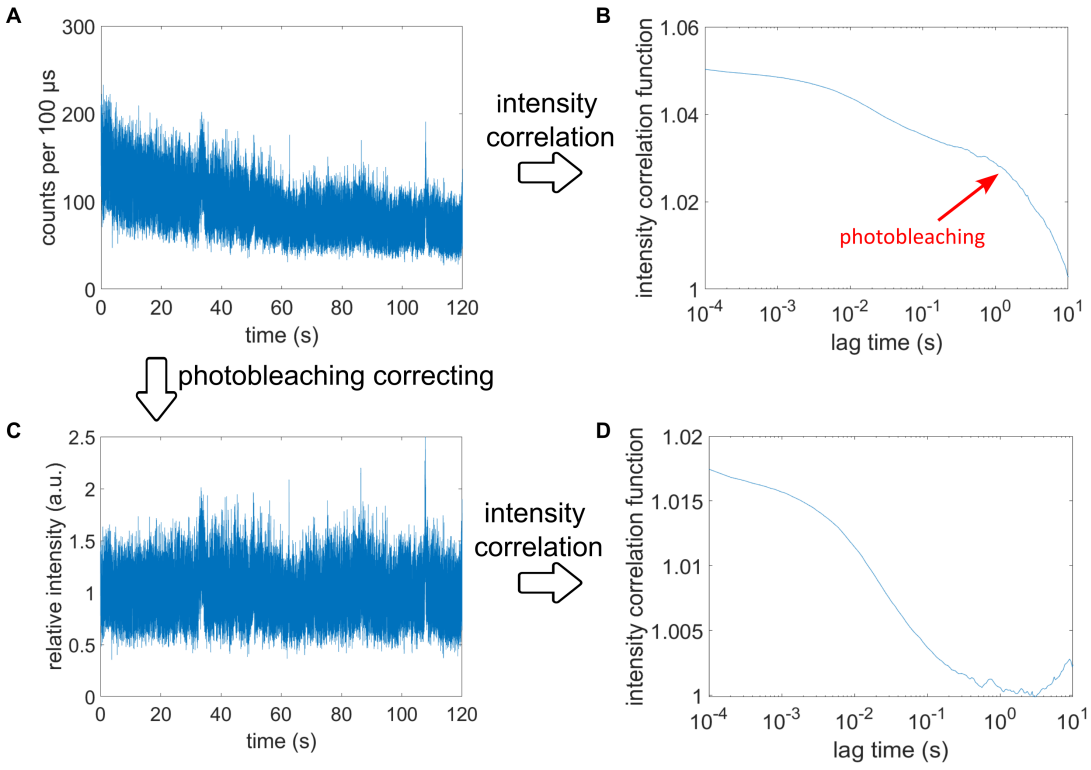

Figure S8: **Photobleaching correction process.** (A) Fluorescence intensity trace measured from the CellMask Deep Red-labeled cell on a MIET substrate. (B) The associated intensity correlation curve is depicted without photobleaching correction. The red arrow indicates the decay component attributed to photobleaching. (C) Fluorescence relative intensity trace after the photobleaching correction. (D) The resulting intensity correlation curve is calculated from the relative intensity trace.

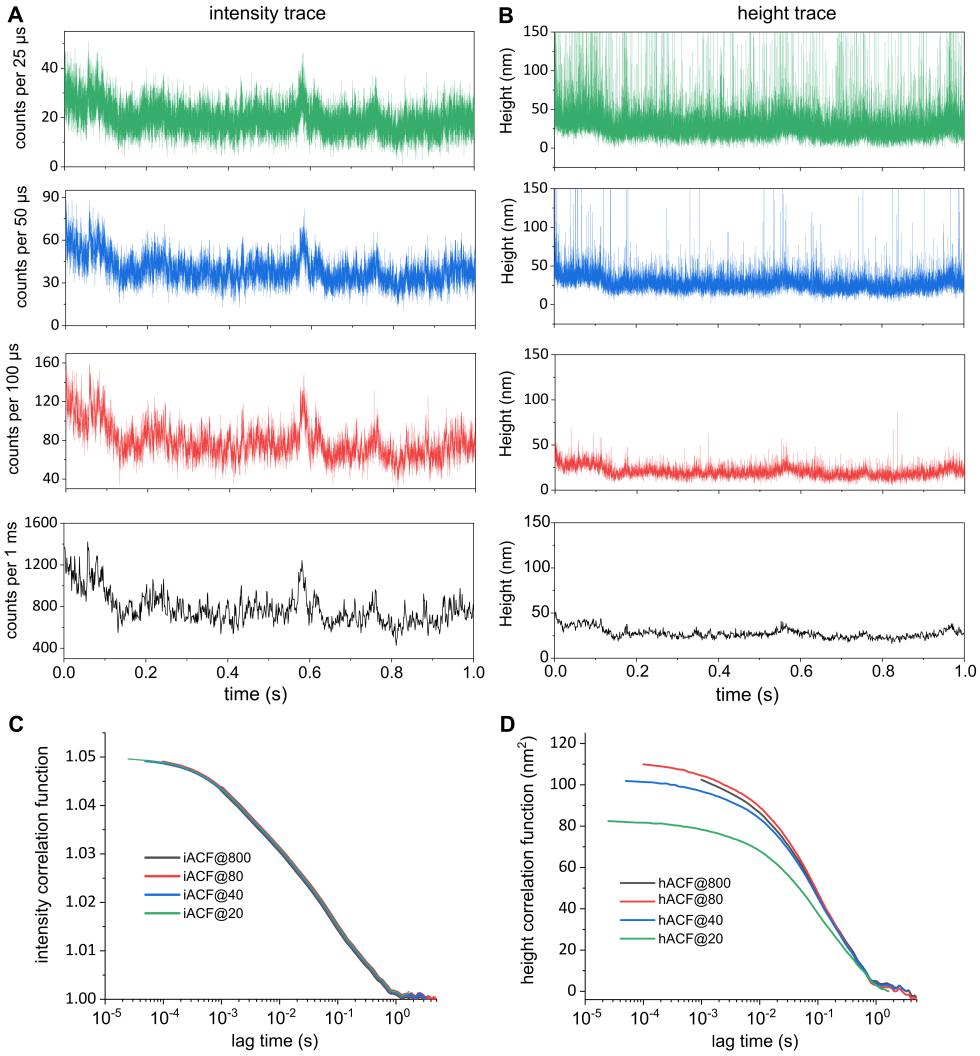

Figure S9: **Determination of temporal resolution.** (A) Fluorescence intensity traces calculated at different time bin widths, and (B) the corresponding height traces. (C) Intensity autocorrelation functions (iACFs) are constructed from different intensity traces as depicted in panel a. The notation 'iACF@800' indicates averaging 800 photons/bin to calculate the iACF, with similar interpretations for other cases. (D) Height autocorrelation functions (hACFs) are constructed from different height traces illustrated in panel b. The amplitude of hACFs at 10^{-3} lag time are: 102.4 nm^2 (hACF@800), 104.5 nm^2 (hACF@80), 96.8 nm^2 (hACF@40), and 78.2 nm^2 (hACF@20), corresponding to the membrane fluctuations ψ are: 10.1 nm^2 (hACF@800), 10.2 nm^2 (hACF@80), 9.8 nm^2 (hACF@40), and 8.8 nm^2 (hACF@20).

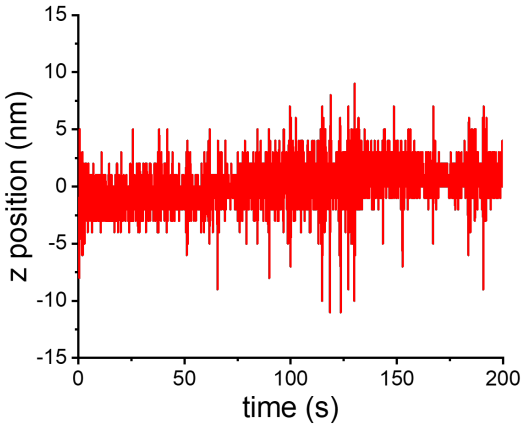

Figure S10: **Axial focus stability during dynaMIET measurements.** Representative time trace of the sample z-position recorded during a typical point FCS/dynaMIET acquisition with the active autofocus system engaged.

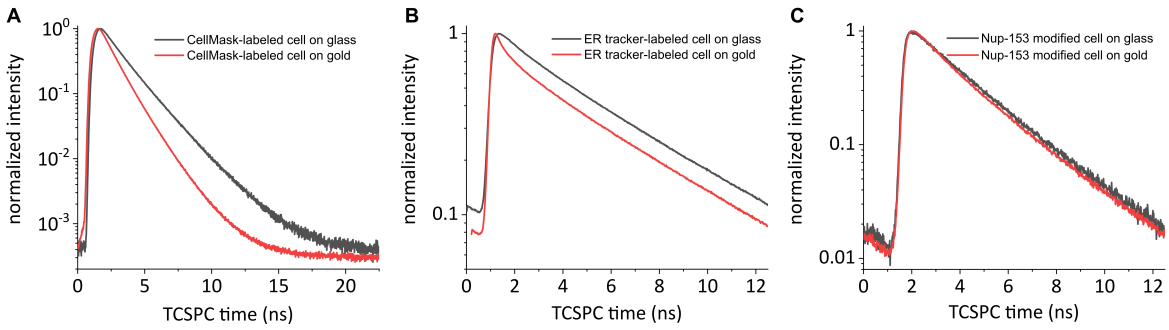

Figure S11: **Fluorescence lifetime decay curve for different samples.** (A) Fluorescence lifetime decay curve for CellMask-Deep-Red-labeled cell on glass and on gold surface. (B) Fluorescence lifetime decay curve for ER-Tracker-Red-labeled cell on glass and on gold surface. (C) Fluorescence lifetime decay curve for eGFP-nup153-modified cell on glass and on gold surface.

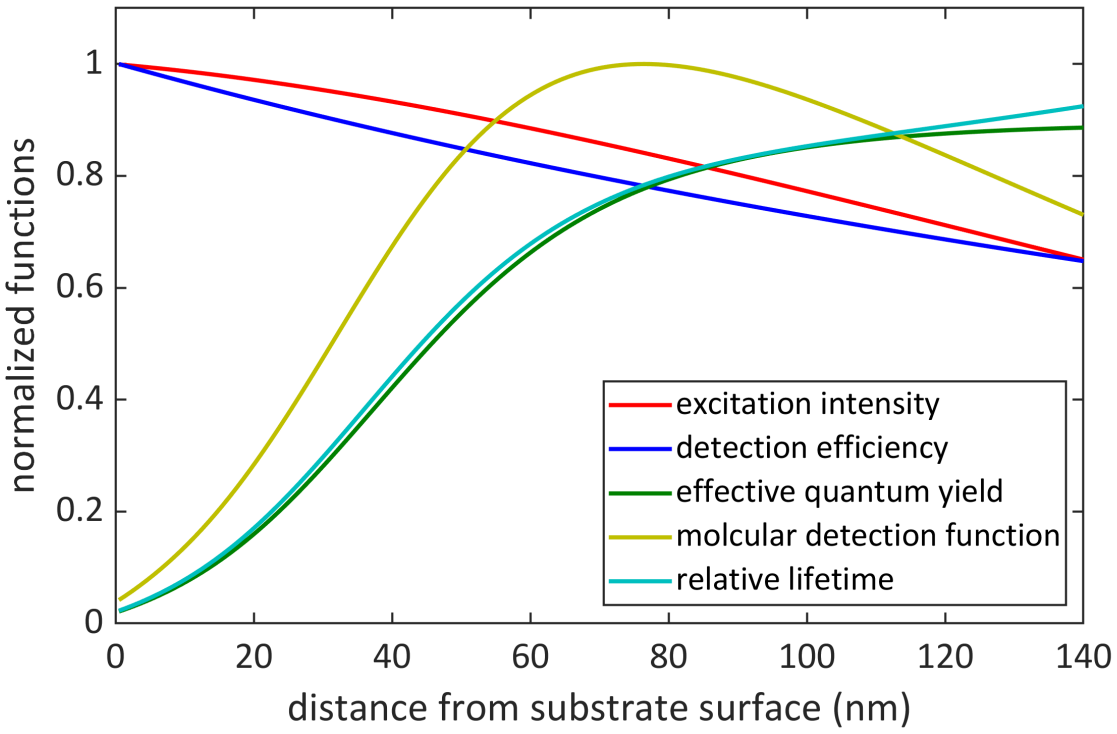

Figure S12: **MIET theoretic calculation.** Calculated excitation intensity, detection efficiency, effective quantum yield, molecular detection function, and relative fluorescence lifetime as a function of the emitter–surface distance h on a MIET substrate. The MIET substrate consists of 2 nm Ti, 10 nm Au, 1 nm Ti, and 10 nm SiO_2. The calculations assume an emitter with a peak emission wavelength of 690 nm, a fluorescence quantum yield of 0.8, and random dipole orientation, excited at 640 nm and detected using an objective with a N.A. of 1.49

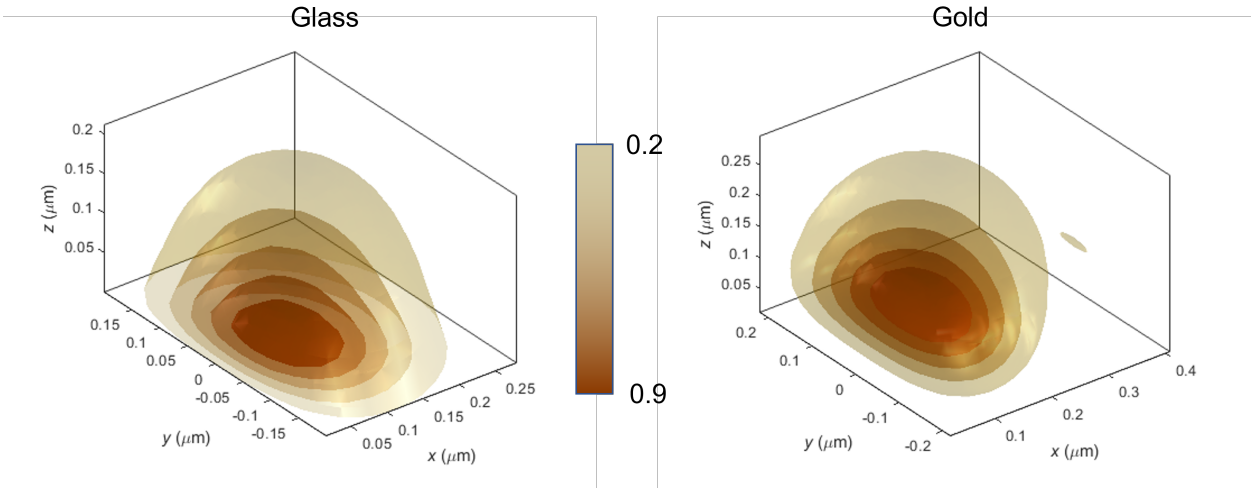

Figure S13: **Brightness iso-surfaces calculation.** Comparison of calculated 3D iso-surfaces of molecular brightness as a function of position within a confocal focus (N.A. = 1.49) of a circular polarized beam, with the focal plane positioned at the glass–sample interface, for both a glass substrate (left) and an MIET substrate (right).